Mon. Not. R. Astron. Soc. **000**, 1–13 () Printed 30 October 2009 (MN LATEX style file v2.2)

VSA Observations of the Anomalous Microwave Emission in the Perseus Region

Christopher T. Tibbs,[1⋆] Robert A. Watson,[1] Clive Dickinson,[1] Rodney D. Davies,[1] Richard J. Davis,[1] Simon Buckmaster,[1] Carlos del Burgo,[2,3] Thomas M. O. Franzen,[4] Ricardo Génova-Santos,[2,5] Keith Grainge,[4,6] Michael P. Hobson,[4] Carmen P. Padilla-Torres,[2] Rafael Rebolo,[2,7] José Alberto Rubiño-Martín,[2,5] Richard D. E. Saunders,[4,6] Anna M. M. Scaife[4] and Paul F. Scott[4]

[1] *Jodrell Bank Centre for Astrophysics, School of Physics and Astronomy, The University of Manchester, Manchester, M13 9PL, UK*
[2] *Instituto de Astrofisíca de Canarias, 38200 La Laguna, Tenerife, Spain*
[3] *UNINOVA/CA3, Campus da FCT/UNL, Qunita da Torre 2829-516 Caparica, Portugal*
[4] *Astrophysics Group, Cavendish Laboratory, J.J. Thomson Avenue, Cambridge, CB3 0HE, UK*
[5] *Dept. of Astrophysics, Unvi. de la Laguna, Tenerife, Spain*
[6] *Kavli Institute for Cosmology, Cambridge, Madingley Road, Cambridge CB3 0HA, UK*
[7] *Consejo Superior de Investigaciones Científicas, Spain*

Received **insert**; Accepted **insert**

ABSTRACT

The dust complex G159.6–18.5 in the Perseus region has previously been observed with the COSMOSOMAS experiment (Watson et al. 2005) on angular scales of $\approx 1^{\circ}$, and was found to exhibit anomalous microwave emission. We present the first high angular resolution observations of this dust complex, performed with the Very Small Array (VSA) at 33 GHz, to help increase the understanding of the nature of this anomalous emission.

On the angular scales observed with the VSA ($\approx 10 - 40'$), G159.6–18.5 consists of five distinct components, all of which are found to exhibit an excess of emission at 33 GHz that is highly correlated with far-infrared emission. Within the region, we find a wide range of physical conditions: one of the features, which is associated with the reflection nebula IC 348, has a dust emissivity comparable to that of HII regions, while the other four features have values in agreement with previous observations of intermediate Galactic latitudes. We provide evidence that all of these compact components have anomalous emission that is consistent with electric dipole emission from very small, rapidly rotating dust grains. We find that these five components contribute ≈ 10 % to the flux density of the diffuse extended emission detected by COSMOSOMAS, implying that the bulk of the anomalous emission in Perseus is diffuse and not concentrated in these compact components.

Key words: radiation mechanisms: general – ISM: individual: G159.6–18.5 – clouds – dust, extinction – radio continuum: ISM

1 INTRODUCTION

With the continuous improvement in experiments to measure the Cosmic Microwave Background (CMB) anisotropies to greater sensitivities, the accurate modelling and subtraction of CMB foregrounds becomes ever more important. Within our own Galaxy, there are three well defined sources of diffuse continuum emission causing foreground contamination: synchrotron and free–free emission, which dominate at frequencies below ≈ 60 GHz; and thermal (vibrational) dust emission, which dominates at higher frequencies. However, there is increasing evidence supporting the existence of an additional continuum emission mechanism in the frequency range $\approx 10 - 60$ GHz (Leitch et al. 1997; Banday et al. 2003; Davies et al. 2006; Hildebrandt et al. 2007; Dobler & Finkbeiner 2008, and references therein).

⋆ E-mail: ctibbs@jb.man.ac.uk (CTT)

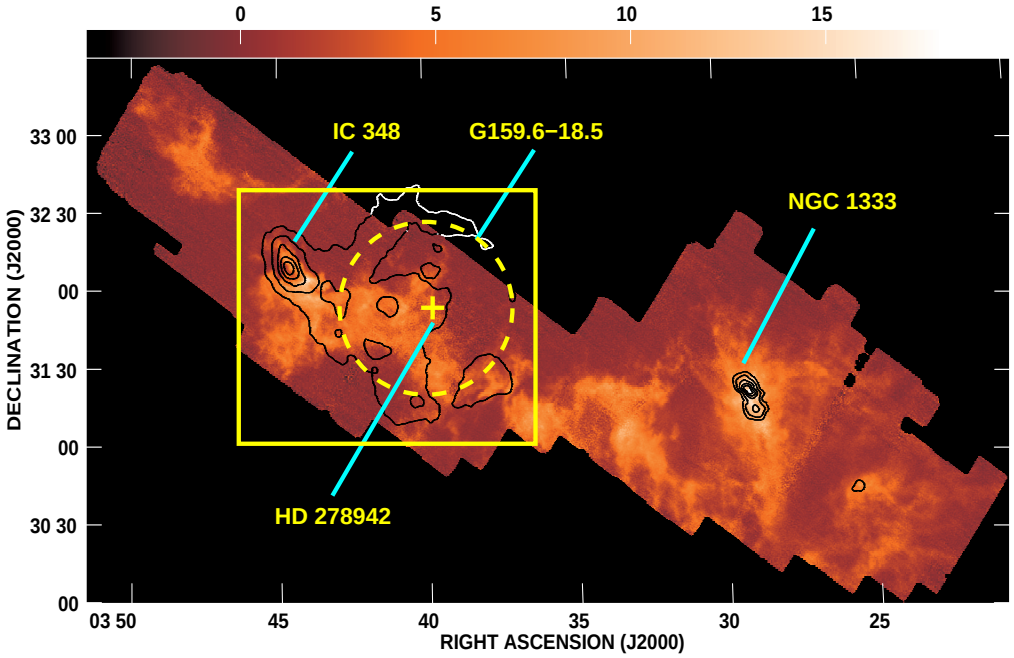

Figure 1. ^{13}CO intensity false colour image (Ridge et al. 2006a) of the Perseus molecular cloud overlaid with contours of the *IRIS* 100 μm emission (10, 20, 40, 60 and 80 % of the peak emission 680 MJy sr^{-1}) showing the location of the dust shell G159.6–18.5 (dashed line), the central star HD 278942 (cross) and the location of 2 major star formation sites, IC 348 and NGC 1333. The box illustrates the region in which the VSA observations were performed.

Various theories have been proposed to explain this "anomalous" emission, including magnetic dipole emission (Draine & Lazarian 1999), hard, flat spectrum, synchrotron emission (Bennett et al. 2003) and bremsstrahlung from very hot ($T_e \sim 10^6$ K), shock heated gas (Leitch et al. 1997). However, the currently favoured emission mechanism is that of very small ($N \leqslant 10^3$ atoms), rapidly rotating ($\sim 1.5\text{x}10^{10}$ s^{-1}) dust grains, emitting electric dipole radiation, commonly referred to as "spinning dust" (Draine & Lazarian 1998; Ali-Haïmoud et al. 2009).

This anomalous emission has been detected on large angular scales across substantial areas of the sky (Kogut et al. 1996; de Oliveira-Costa et al. 1997, 1999, 2002; Miville-Deschênes et al. 2008) and also on small angular scales in specific Galactic objects, such as LDN 1622 (Finkbeiner et al. 2002; Finkbeiner 2004; Casassus et al. 2006), G159.6–18.5 (Watson et al. 2005), RCW 175 (Dickinson et al. 2009), LDN 1111 (AMI Consortium; Scaife et al. 2009a) and a number of Lynds Dark Nebulae (AMI Consortium; Scaife et al. 2009b) and is often found to be tightly correlated with the far-infrared (FIR) emission.

One of these Galactic objects, G159.6–18.5, is located within the Perseus molecular complex. Observations performed with the COSMOSOMAS experiment (Watson et al. 2005) identified a bright source of dust-correlated emission at $\approx 20 - 30$ GHz, with a peaked spectrum, indicative of spinning dust. This is perhaps the best example of a peaked spectrum that is well fitted by a Draine & Lazarian (1998) spinning dust model. These results prompted further investigations of this region, which were performed with the Very Small Array (VSA), a 14-element interferometric array operating at 33 GHz; Watson et al. (2003) describe the nominal VSA setup. In the present paper we present and discuss our results from these new observations. Section 2 describes the region under investigation and presents the VSA observations, while Section 3 details the data reduction. Section 4 discusses the available ancillary data, which were used to help gain a better understanding of the physical conditions within the region. In Section 5 we produce spectral energy distributions (SEDs) for 5 features in the region. In Section 6 we analyse these SEDs and the relationship between our VSA results and the COSMOSOMAS results (Watson et al. 2005). Finally, our conclusions are discussed in Section 7.

Table 1. Summary of the characteristics of the VSA in the super-extended array configuration.

Location	Teide Observatory
Altitude	2400 m
Latitude	$+28^o\ 18'$
Declination range	$-7^o < \text{Dec} < +63^o$
No. of antennas (baselines)	14 (91)
No. of correlations	182
T_{sys} (K)	≈ 35
Frequency (GHz)	33
Bandwidth (GHz)	1.5
Primary beam FWHM (arcmin)	72
Synthesized beam FWHM (arcmin)	≈ 7
Sensitivity (mJy beam^{-1} in 50 hrs)	≈ 5

2 VSA OBSERVATIONS OF G159.6–18.5

2.1 The G159.6–18.5 Region

The Perseus molecular complex is a giant molecular cloud located in the Perseus constellation at a distance of ~ 260 pc (Cernicharo, Bachiller & Duvert 1985). The cloud chain is ~ 30 pc in length and contains many well known sites of active star formation. The feature observed by Watson et al. (2005), G159.6–18.5, appears as a remarkably complete dust shell of enhanced FIR emission with diameter $\approx 1^{\circ}.5$ as shown in Fig. 1.

Fig. 1 displays a ^{13}CO intensity image (Ridge et al. 2006a) illustrating the extent of the Perseus molecular cloud. Overlaid on the image are contours of the *IRIS*[1] 100 μm emission showing the location of the dust shell G159.6–18.5, which does not appear to be traced by the ^{13}CO emission. Also overlaid is a rectangle showing the coverage of the VSA observations.

Due to its shape, G159.6–18.5 was initially believed to be a supernova remnant (Pauls & Schwartz 1989; Fiedler et al. 1994), but more recent observations have determined that the source of the shell is the O9.5–B0V star, HD 278942, at its geometric centre, and that the shell is filled with HII gas (Andersson et al. 2000). Observations performed as part of the COMPLETE Survey (Ridge et al. 2006b) suggested that G159.6–18.5 was indeed an expanding HII bubble located on the far side of the molecular cloud. The distribution of the ionized gas will be discussed in more detail in Section 4.1.

2.2 VSA Observations

The VSA is a CMB interferometer, situated at an altitude of 2400 m at Teide Observatory, Tenerife. It has been used to measure the CMB angular power spectrum for multipole values in the range $150 \leqslant \ell \leqslant 1500$ (Scott et al. 2003; Grainge et al. 2003; Dickinson et al. 2004).

The observations of the dust feature G159.6–18.5 were performed during the period September 2005 to July 2008 at 33 GHz with the "super-extended" array configuration[2]. Table 1 provides a summary of the super-extended VSA characteristics. Observations of calibration sources have shown that the VSA interferometric pointing accuracy is better than $1'$.

Due to its size ($\approx 2^{\circ} \times 1^{\circ}$), the G159.6–18.5 dust feature was observed with 11 different pointings, each with a primary beam of $1^{\circ}.2$ full width at half maximum (FWHM). Each one of the 11 pointings were repeated numerous times, and were then combined to provide the best possible *u,v*-coverage. This *u,v*-coverage limits the VSA to observing structure on scales $\approx 10 - 40'$, and hence our observations resolve out any larger scale emission. To observe this larger scale structure, one would need to use single dish observations with a $\approx 40'$ beam. Table 2 provides a summary of the 11 pointings, including the total observing time and r.m.s. noise for each pointing. These r.m.s. noise values will be discussed in Section 3.2.

Table 2. Summary of the VSA observations.

Pointing	RA (J2000)	DEC (J2000)	Total Obs. Time (hr)	R.M.S. Noise (mJy beam^{-1})
A	03:41:24	+32:03:28	≈ 50	13.3
B	03:46:00	+32:03:28	≈ 20	16.4
C	03:44:12	+32:03:28	≈ 30	14.1
D	03:42:48	+32:39:50	≈ 65	16.4
E	03:40:00	+32:39:50	≈ 25	19.7
F	03:38:36	+32:03:28	≈ 25	13.9
G	03:40:00	+31:27:06	≈ 30	12.0
H	03:42:48	+31:27:06	≈ 25	14.0
I	03:33:32	+31:34:33	≈ 45	19.3
J	03:37:12	+32:39:50	≈ 25	30.6
K	03:37:12	+31:27:06	≈ 20	26.8

3 VSA DATA

3.1 Data Reduction and Calibration

The VSA data reduction and calibration were performed using the software tool REDUCE. This software was specifically designed for use with VSA data and is described in detail in Dickinson et al. (2004) and references therein. Flux density calibration was applied using Tau A with a flux density of 350 Jy at 33 GHz. This value was determined from observations with the VSA extended array (Hafez et al. 2008) using Jupiter as the "absolute" calibrator with $T_b = 146.6 \pm 0.75$ K at 33 GHz based on *WMAP* observations (Hill et al. 2009). Tau A was chosen due to its proximity ($\approx 26^{\circ}$ away on the sky), which meant that both the target and calibrator were available at the same time of day. Short observations of the calibrator (≈ 10 mins) allowed us to use Tau A as both a flux density and phase calibrator. Uncertainties due to phase drifts and atmospheric/gain errors are typically less than a few percent. Throughout the paper we have assumed a conservative absolute calibration uncertainty of 5 %.

In addition to performing the flux density and phase calibration, REDUCE automatically performs much of the data editting by flagging antennas and baselines that were noisy or not working correctly. REDUCE also allows the user to filter out any contaminating signals such as bright sources (e.g. Sun, Moon etc.) passing through the side lobes of the VSA beam. This fringe-rate filtering is described in detail in Watson et al. (2003). After this filtering had been performed, the data were fringe-rotated to the centre of the field, and calibrated. All the data were inspected and reduced individually, and a *u,v* visibility file for each observation was produced.

3.2 VSA Map

All the *u,v* data for each pointing were combined to form a single *u,v* visibility file for each one of the 11 point-

[1] Improved Reprocessing of the *IRAS* Survey (Miville-Deschênes & Lagache 2005).
[2] The "super-extended" array configuration was the third and final array configuration for the VSA. Previously the "compact" and "extended" array configurations were in operation.

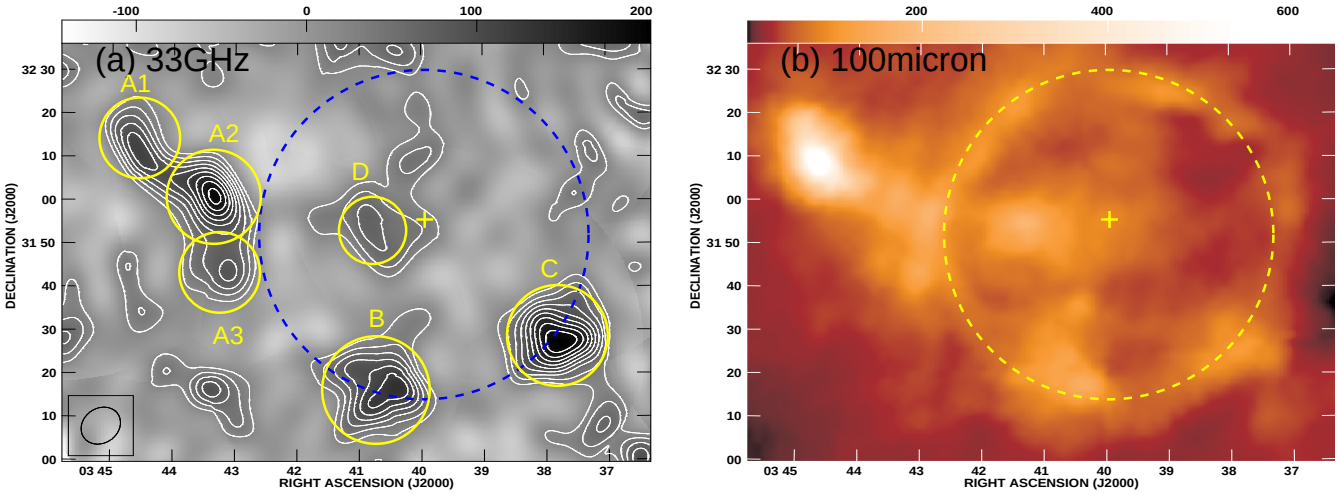

Figure 2. G159.6–18.5 as observed with the VSA at 33 GHz (left) and *IRIS* 100 μm (right). The location of the dust shell (dashed line), the O9.5–B0V star, HD 278942 (cross), and the position of the 6 features in the VSA image (A1, A2, A3, B, C and D) are indicated. The 5 features in the VSA map, with high signal-to-noise ratios (A1, A2, A3, B and C), are discussed and analysed throughout the rest of the present paper. The central feature, D, with a much lower signal-to-noise ratio, was not included in our analysis, but will be discussed in Section 4.2. The VSA $\approx 7'$ FWHM synthesized beam is shown in the bottom left-hand corner of the image, and the contours correspond to 10, 20, 30, 40, 50, 60, 70, 80, 90 % of the peak flux which is 200 mJy beam^{-1}. The units of the *IRIS* image are MJy sr^{-1}.

Table 3. Position, flux density, deconvolved angular size and position angle of the 6 features observed with the VSA at 33 GHz.

Feature	RA (J2000)	DEC (J2000)	Flux Density (Jy)	Major Axis (arcmin)	Minor Axis (arcmin)	Position Angle (deg)
A1	03:44:30	+32:11:27	0.53 ± 0.12	21.6 ± 4.4	4.4 ± 3.8	27.8 ± 7.9
A2	03:43:27	+32:00:17	1.39 ± 0.20	24.3 ± 3.1	12.0 ± 2.2	33.2 ± 8.3
A3	03:43:14	+31:46:25	0.37 ± 0.13	16.1 ± 5.8	9.8 ± 5.4	2.6 ± 36.9
B	03:40:41	+31:16:31	1.23 ± 0.21	20.5 ± 4.8	17.6 ± 4.8	30.1 ± 44.5
C	03:37:49	+31:27:57	0.86 ± 0.14	14.0 ± 3.1	13.5 ± 2.9	131.0 ± 35.1
D	03:40:49	+31:54:38	0.18 ± 0.10	16.0 ± 9.1	4.9 ± 5.7	20.0 ± 32.3

ings. A clean map was then created for each pointing using the AIPS[3] task IMAGR, which uses a CLEAN based algorithm (Högbom 1974). A small loop gain (0.05) was used in the cleaning process to help retain the extended emission. Typical values of the r.m.s. noise in these images is ≈ 12 – 30 mJy beam^{-1} (Table 2). These r.m.s. values were calculated outside the primary beam for each image, and show that the observations are not dominated by thermal noise, but rather by the dynamic range of the data and residual deconvolution effects. An additional contribution to the r.m.s. noise in these images arises from the CMB anisotropies; calculated to be ≈ 5 mJy beam^{-1} on these angular scales.

A mosaic of all the pointings was then created using the AIPS task LTESS, which linearly combines the pointings and applies a primary beam correction in the image plane. This primary beam correction was applied out to a radius of $\approx 1^\circ$ for each individual image. The final VSA map is shown in Fig. 2a with 5 features, all with a high signal-to-noise ratio, identified (A1, A2, A3, B and C). The central feature, D, in Fig. 2a has a much lower signal-to-noise ratio, and as such was not included in our analysis but it will be discussed in Section 4.2.

The *IRIS* 100 μm image of G159.6–18.5 (Fig. 2b) traces the big grain dust emission in the FIR, where the dust shell is observed. One can identify that the shell consists of a few main features. Comparing Fig. 2a with Fig. 2b, one can see that the features observed at 33 GHz are closely correlated with the denser dust clumps in G159.6–18.5, but not with the ring structure, which does not appear in the VSA map. The spatial structure and their implications will be discussed in further detail in Section 4.

The flux density in the 6 features shown in Fig. 2a was calculated by simultaneously fitting an unconstrained elliptical gaussian component and a baseline offset to each feature individually using the AIPS task JMFIT. The fitted gaussian components accounted for ≈ 99 % of the flux in the features. The fitting error from JMFIT, along with the absolute calibration error of the VSA were added in quadrature to determine the final error. Table 3 lists the position, integrated flux density, deconvolved angular size and position angle of the fitted gaussian component for all 6 features.

[3] Astronomical Image Processing System.

4 ANCILLARY DATA

Due to its size and range of physical conditions, the Perseus molecular complex is a well-studied region, and therefore there is a wide variety of ancillary data available, which we used to help with our analysis (Table 4). Fig. 3 displays the ancillary data[4] overlaid with the VSA contours at 33 GHz.

4.1 Radio Frequency Data

At frequencies below $\approx$ 60 GHz, the emission is expected to be dominated by synchrotron and free–free emission. However, since G159.6–18.5 is far from the Galactic plane ($l = 159°.6$ and $b = -18°.5$) and not in the vicinity of any known supernova remnants, the synchrotron emission is expected to be negligible at 33 GHz. Therefore the radio frequency ancillary data help us to understand the free–free emission.

In the Stockert 1.4 GHz survey (Fig. 3a), one can identify a region of diffuse emission within the shell that is offset from the centre by $\approx$ 10 - 15′. This diffuse region of $\approx$ 40 arcmin diameter has also been mapped at 2.7 GHz by Reich & Reich (2009). There appears to be little or no emission at 1.4 GHz from the 5 features observed at 33 GHz with the VSA. This agrees with the current understanding of the region, which is believed to contain a bubble of HII gas within the dust shell. The Hα image (Fig. 3b) appears to confirm this hypothesis, with the Hα emission also being confined to the interior of the shell, and also offset similar to the Stockert observations, which we would expect as it traces the hot ($T_e \sim 10^4$ K) ionized gas.

The NRAO VLA Sky Survey (NVSS) at 1.4 GHz and the GB6 4.85 GHz survey (Fig. 3c and Fig. 3d respectively) have much higher resolution than both the Stockert survey and the VSA observations, and are very useful for identifying compact radio sources, including HII features. We find three radio sources in the G159.6–18.5 region: 4C 31.14 to the south–east of the ring; 3C 92 within the ring; and 4C 32.14 to the north–west of the ring. All these sources are extra-galactic with spectral indices[5] of $\alpha \approx -0.7$, -1.0 and -0.03 respectively. The flat spectrum quasar 4C 32.14 was removed from the VSA map by subtracting a CLEAN component model from the UV data. All 5 features observed with the VSA, however, appear to be free from any source contamination. Extra-galactic source counts at 15 GHz (Waldram et al. 2003) imply that the 30 GHz extra-galactic source population cannot remotely account for the 5 observed features. Also the fact that the features we observe are extended, strongly rules out the possibility of significant extra-galactic source contamination.

Weak large scale emission, predominantly resolved out, can be seen within the shell in the GB6 image, and is aligned with the Stockert survey observations. However, this large scale diffuse emission does not extend as far as the 5 features observed with the VSA.

[4] Data were downloaded from the *Skyview* website (http://skyview.gsfc.nasa.gov), the LAMBDA website (http://lambda.gsfc.nasa.gov) and the COMPLETE Survey website (http://www.cfa.harvard.edu/COMPLETE).

[5] Throughout this paper, the flux density spectral index is defined as $S_\nu \propto \nu^\alpha$.

Table 4. Summary of the ancillary data used in our analysis. References are: [1] Reich & Reich (1986); [2] Finkbeiner (2003); [3]: Condon et al. (1998); [4] Condon, Broderick & Seielstad (1989); [5] Ridge et al. (2006a); [6] Hinshaw et al. (2009); [7] Miville-Deschênes & Lagache (2005).

Telescope/ Survey	Frequency/ Wavelength	Angular Resolution	Ref.
Stockert	1.4 GHz	34′	[1]
WHAM/VTSS/SHASSA	Hα	6′	[2]
NVSS	1.4 GHz	0′.75	[3]
GB6	4.85 GHz	3′.5	[4]
2MASS/NICER	Av	5′	[5]
WMAP	94 GHz	12′.6	[6]
IRAS/IRIS	12 μm	3′.8	[7]
IRAS/IRIS	25 μm	3′.8	[7]
IRAS/IRIS	60 μm	4′.0	[7]
IRAS/IRIS	100 μm	4′.3	[7]

The visual extinction (Av) map (Fig. 3e) shows that the extinction is quite high throughout the entire region ($\approx$ 2 – 10 mag), suggesting a large quantity of dust in the vicinity. This makes it very difficult to calculate the free–free emission using the Hα emission, as it is unclear what fraction of the extinguishing dust is situated between us and the molecular cloud. However, to establish whether or not the emission in the VSA map could be due entirely to free–free emission, we calculated an estimate of the associated Hα emission assuming that all the emission observed with the VSA at 33 GHz was due to free–free emission, based on an electron temperature $T_e \approx 7000$ K (Dickinson et al. 2003). Using the conservative assumption that all the extinguishing dust is located between us and G159.6–18.5, we find that an upper limit estimate of the actual Hα emission is much too faint (typically on average by a factor of 20) to account for the observed 33 GHz emission. In Section 5.1.1 we present a more rigorous analysis that constrains the level of free–free emission observed with the VSA.

4.2 Higher Frequency Data

Emission at higher frequencies ($\geqslant$ 60 GHz) is dominated by thermal dust emission. The *WMAP* 5-yr total intensity W-band map and the *IRIS* 100, 60, 25 and 12 μm maps were used to enable us to understand this emission. The *WMAP* W-band (94 GHz) image (Fig. 3f) is believed to trace the large, cold ($T < 15$ K) dust grains and shows that there is emission on large angular scales in the central region of G159.6–18.5. Comparing Fig. 3e with Fig. 3f identifies that these large, cold dust grains are causing the extinction.

The *IRIS* images in Fig. 4 display the emission in the FIR, where the emission is generally interpreted as due to three dust components: big grains (BGs), very small grains (VSGs) and polycyclic aromatic hydrocarbons (PAHs), deduced from IRAS observations (Desert et al. 1990). Fig. 4 also highlights the high degree of correlation between the emission at microwave and FIR wavelengths. A Pearson correlation analysis was performed in the image plane within apertures centred on each feature. The apertures were chosen to be large enough to include a background contribution, but not so large as to have any overlapping apertures. We

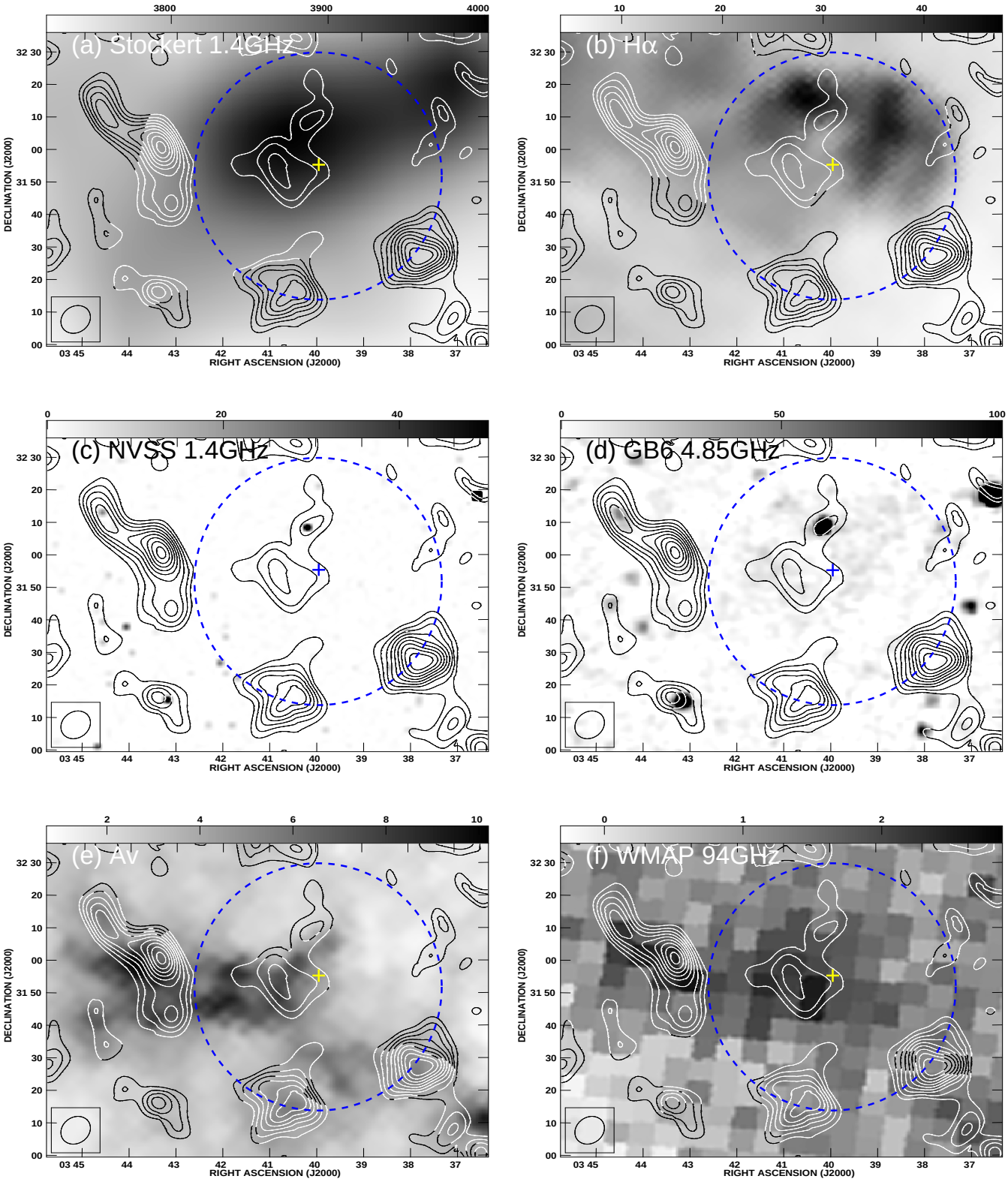

Figure 3. Ancillary data overlaid with the VSA contours and synthesized beam, as shown in Fig. 2a, displaying maps of G159.6-18.5 at various wavebands in grey scale: a) Stockert 1.4 GHz in units of mK (T_b); b) Hα in units of R; c) NVSS 1.4 GHz in units of mJy beam^{-1}; d) GB6 4.85 GHz in units of mJy beam^{-1}; e) Av in units of mag; f) *WMAP* 94 GHz in units of Jy beam^{-1}. The dashed line displays the position of the dust shell, and the cross marks the position of the central star, HD 278942.

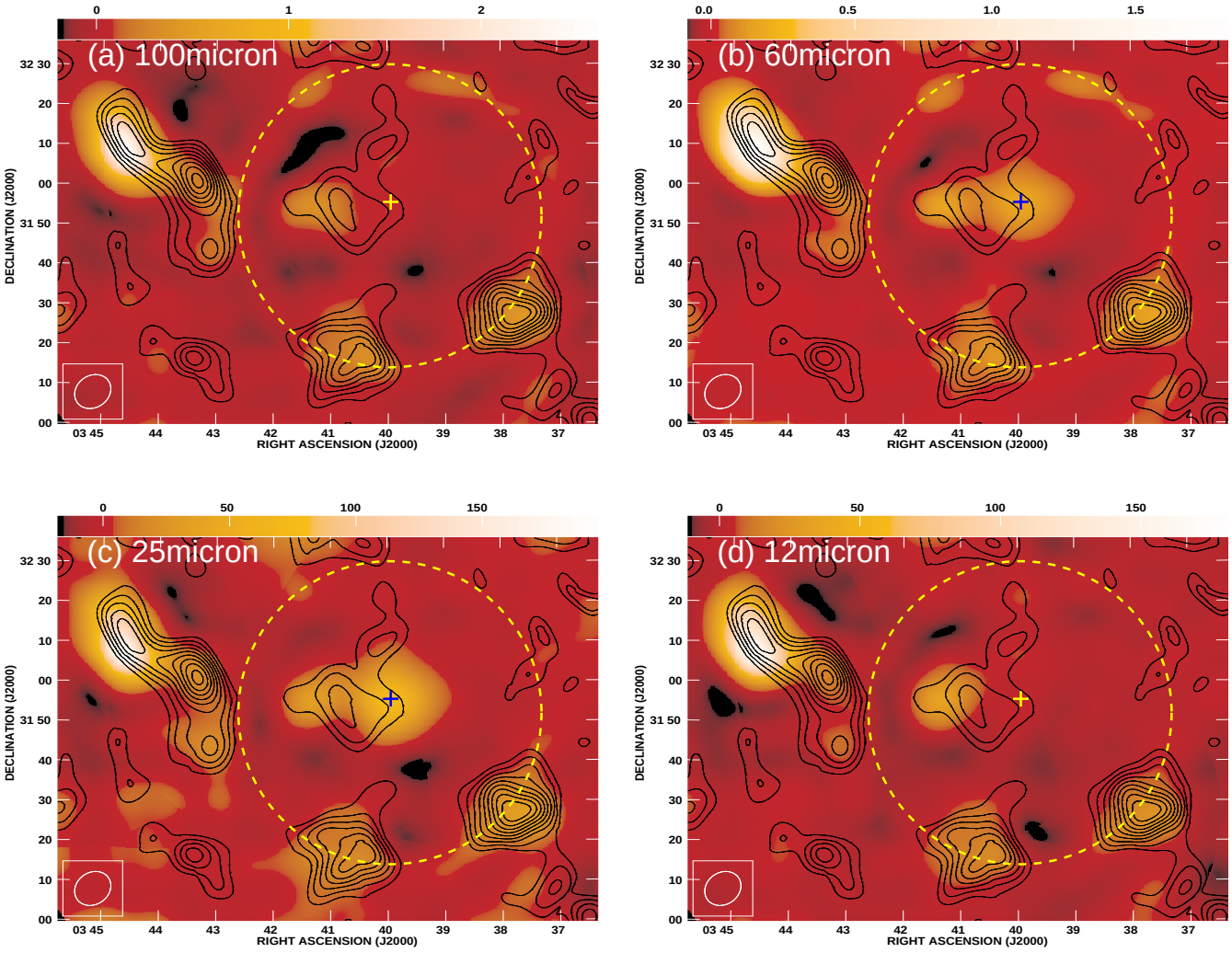

Figure 4. False colour *IRIS* images of G159.6–18.5 processed with the VSA sampling distribution (see Section 5.1.2) overlaid with the VSA contours and synthesized beam, as shown in Fig. 2a: a) *IRIS* 100 μm in units of kJy beam^{-1}; b) 60 μm in units of kJy beam^{-1}; c) 25 μm in units of Jy beam^{-1}; d) 12 μm in units of Jy beam^{-1}. The dashed line displays the position of the dust shell, and the cross marks the position of the central star, HD 278942. These images highlight the correlation between the emission at microwave and FIR wavelengths.

found that there is indeed a high degree of correlation between the FIR emission and the microwave emission, with a mean Pearson correlation coefficient of ≈ 0.80 across all the features and all the *IRIS* bands. This correlation does not occur throughout the entire region as we find a mean correlation coefficient of ≈ 0.17 for an aperture well away from any of the 5 features. These results imply that the correlation between the FIR emission and the microwave emission is concentrated in the 5 features observed with the VSA. Further investigation of this correlation, using data from the *Spitzer Space Telescope*, will be performed in a follow-up paper.

The region in the centre of the dust shell is interesting as there appear to be two distinct FIR components, offset by $\approx 20'$. One component to the east, which is visible in all 4 *IRIS* bands, and another more central component that appears to peak at ≈ 60 μm, suggestive that this is much warmer (T $\approx$ 70 K) than the surrounding dust (T $\approx$ 30 – 40 K as displayed on the plots in Fig. 5). From Fig. 4b and Fig. 4c, one can see that the location of the O9.5–B0V star, HD 278942, corresponds to the brighter central component, and hence this could be acting as a heat source for the dust, and therefore producing the higher dust temperatures observed locally.

5 SPECTRAL ENERGY DISTRIBUTIONS OF THE 5 REGIONS

To identify whether the emission observed in the VSA map is actually anomalous, we produced a spectrum to determine whether there was an excess over the level of free–free and thermal dust emission. To constrain the levels of free–free emission we used the GB6 4.85 GHz observations (Section 5.1.1), and to constrain the levels of thermal dust emis-

sion we used the *IRIS* observations in the FIR regime (Section 5.1.2) and the *WMAP* W-band data in the Rayleigh–Jeans regime (Section 5.1.3).

5.1 Integrated Flux Density Spectra of Individual Features

5.1.1 GB6

As discussed in Section 2.2, the VSA only observes structures on angular scales of $\approx 10 - 40'$. Therefore, to determine the level of free–free emission in the VSA map, we need some low frequency observations with a similar angular resolution, namely, observations with an equivalent range of *u,v*-coverage. None of the three available low frequency surveys discussed in Section 4.1 provide an ideal match for the VSA. The Stockert survey cannot be used due to the lack of short spacings in the VSA coverage, where all the large scale structure has been resolved out and the NVSS also suffers from an absence of short-spacings, which makes it unsuitable. This leaves the GB6 survey.

The original GB6 observations have been filtered to remove all structure on scales larger than $\approx 20'$ (Condon, Broderick & Seielstad 1989) and hence cannot be used directly to assess the levels of free–free emission in the VSA image. To allow us to make use of the GB6 image, we had to filter the VSA image so as to harmonise the *u,v* ranges sampled. This involved removing all the short ($\leqslant 172\ \lambda$) VSA baselines. The VSA sampling distribution was then applied to the GB6 image using the AIPS task UVSUB. This produces a *u,v* visibility file that has been sampled with the VSA sampling distribution, but with the GB6 visibilities. This was then CLEANed using the AIPS task IMAGR in a similar manner to the VSA image, creating a new re-sampled GB6 image, which allowed us to determine the contribution of free–free emission on these angular scales.

The flux density of the 5 features in the filtered VSA image was calculated using JMFIT to apply both an unconstrained elliptical gaussian and baseline component and is given in Table 5. As discussed in Section 4.1, all the features in the VSA image appear to show no detectable emission in the GB6 image, therefore, using the results of JMFIT on the filtered VSA image, along with the r.m.s. noise in the same region of the re-sampled GB6 image, a 3σ upper limit for the integrated flux density at 4.85 GHz, in each feature, was determined. This is a conservative upper limit since we are dealing with integrated fluxes rather than with peak surface brightnesses.

Table 5 lists the integrated flux density for the 5 features at 4.85 GHz and 33 GHz. The 3σ flux density upper limit at 4.85 GHz has been scaled to 33 GHz, using a nominal free–free spectral index of $\alpha = -0.12$ (Dickinson et al. 2003). A direct comparison between the emission found in the GB6 and VSA images is given as a percentage in the last column in Table 5. This suggests that the contribution of free–free emission at 33 GHz is far from dominant. Assuming that this ratio between the 4.85 GHz and the 33 GHz emission is independent of angular scale, we can compute an estimate for the contribution of free–free emission at 33 GHz on the angular scales of the unfiltered VSA image.

Table 5. Upper limits to the free–free emission in the 5 features. A 4.85 GHz 3σ flux density upper limit based on the GB6 image. This flux density is scaled to 33 GHz using a nominal free–free spectral index of $\alpha = -0.12$. The last column represents the upper limits of free–free emission observed with the VSA at 33 GHz.

Feature	GB6 $S_{4.85\ GHz}$ (mJy)	GB6 $S_{33\ GHz}$ (mJy)	Filtered VSA $S_{33\ GHz}$ (mJy)	% due to free–free (3σ)
A1	< 68.3	< 54.3	178 ± 52	< 31
A2	< 38.8	< 30.8	155 ± 41	< 20
A3	< 32.9	< 26.2	167 ± 56	< 16
B	< 41.0	< 32.6	354 ± 69	< 9
C	< 43.1	< 34.2	95 ± 38	< 36

5.1.2 IRIS

The 4 *IRIS* images at 100, 60, 25 and 12 μm have comparable resolution to the VSA image (Table 4). The VSA sampling distribution was applied to the *IRIS* images using the AIPS task UVSUB in a similar manner to the GB6 image, described in Section 5.1.1. These new *IRIS* images, which are shown in Fig. 4, can then be directly compared with the VSA image. To calculate the flux density of the 5 features in these newly re-sampled images, a constrained fit in which the position and size of the gaussian component was fixed at the parameters obtained from the fits on the VSA image, was applied using JMIFT.

5.1.3 WMAP W-band

The 5-yr *WMAP* W-band map was used to constrain the Rayleigh–Jeans tail of the thermal dust emission. As discussed in Section 4.2 most of the emission at 94 GHz occurs within the central region of G159.6–18.5, and extends to IC 348. To calculate the flux density of all 5 features at 94 GHz, the VSA image was smoothed to a $12'.6$ resolution, and then using JMFIT all the features were fitted with an unconstrained elliptical gaussian and baseline component. The size and position of these gaussians were then kept fixed, and fitted for in the *WMAP* W-band image.

5.2 SED Determination

The flux densities for all 5 features at 4.85 GHz, 33 GHz, 94 GHz, 100 μm and 60 μm are listed in Table 6, and the corresponding flux density spectra are plotted in Fig. 5. From our discussion in Section 4, we know that free–free emission occurs at the radio frequencies, and thermal (vibrational) dust is expected to occur at FIR wavelengths.

We determined an upper limit for the free–free emission at 4.85 GHz, and since we know that a typical free–free emission spectrum follows a power-law with spectral index $\alpha = -0.12$, we plotted this normalized to our upper limit at 4.85 GHz. We note that at frequencies below ≈ 1 GHz, the free–free emission can become optically thick ($\tau > 1$) with a spectral index of $\alpha \approx +2$, but at higher frequencies, the free–free emission becomes optically thin ($\tau \ll 1$) and follows the standard power-law with spectral index $\alpha = -0.12$.

For the thermal dust emission, we used a modified black-body curve function, $\nu^{\beta_{dust}+2}\mathrm{B}(\nu,\mathrm{T}_{dust})$, where β_{dust}

Table 6. Integrated flux density for all 5 features identified in the VSA map at 4.85 GHz, 33 GHz, 94 GHz, 100 μm and 60 μm. All errors quoted include a fitting error and an absolute calibration error (5 % for VSA, 5 % for *WMAP* data and 10 % for the *IRIS* data) combined in quadrature. The residual r.m.s. of each fit is quoted in parentheses. †Flux density at 4.85 GHz is a conservative 3σ upper limit based on the GB6 image (see Section 5.1.1 for details).

Feature	$S_{4.85\ GHz}{}^{\dagger}$ (Jy)	$S_{33\ GHz}$ (Jy)	$S_{94\ GHz}$ (Jy)	$S_{100\ \mu m}$ (Jy)	$S_{60\ \mu m}$ (Jy)
A1	< 0.20	0.53 ± 0.12 (0.01)	0.65 ± 0.63 (0.44)	5000 ± 560 (550)	3200 ± 330 (390)
A2	< 0.35	1.39 ± 0.20 (0.02)	1.99 ± 0.89 (0.43)	2200 ± 460 (210)	810 ± 160 (100)
A3	< 0.07	0.37 ± 0.13 (0.01)	0.34 ± 0.55 (0.41)	770 ± 260 (50)	260 ± 90 (10)
B	< 0.14	1.23 ± 0.21 (0.02)	0.75 ± 1.48 (0.29)	2500 ± 520 (50)	850 ± 170 (20)
C	< 0.39	0.86 ± 0.14 (0.01)	< 1.49 (0.32)	1800 ± 440 (40)	330 ± 110 (20)

is the dust emissivity index and $B(\nu,T_{dust})$ is the black-body function for a dust temperature, T_{dust}. A single temperature dust component, modelled by this modified black-body curve, was fitted to the 94 GHz, 100 μm and 60 μm data points for each feature individually. The best-fitting values for both β_{dust} and T_{dust} are displayed on the plots in Fig. 5.

Also plotted in Fig. 5 are the 25 and 12 μm data points. These were not fitted by the single temperature modified black-body curve because the emission at these wavelengths is not due to the same dust grain population as the 100 and 60 μm. The 100 and 60 μm emission is dominated by BGs, while the 25 and 12 μm emission is dominated by VSGs. The 12 μm emission has an additional contribution from PAHs.

6 DISCUSSION

6.1 SED Modelling

In each plot in Fig. 5, it is possible to identify an excess of emission present at 33 GHz that cannot be explained by either free–free or thermal dust emission. This fraction of excess emission ($f_{33\ GHz}$), and the corresponding significance, are displayed on the plots in Fig. 5.

For features A1, A2, A3 and B, the 94 GHz data point provides a constraint on the shape of the thermal dust curve, providing the best-fitting values for the dust temperature T_{dust}, and the dust emissivity index, β_{dust} (see plots in Fig. 5). However, for feature C, the 94 GHz data point is an upper limit and hence does not provide a reliable constraint on the thermal dust curve. Therefore, for this feature, we used a fixed value of $\beta_{dust} = 1.5$. This is a typical value of β_{dust} (Dupac et al. 2003), and to ensure that selecting this value was reasonable, we investigated using a value of $\beta_{dust} = 1.1$ (towards the lowest measured value for β_{dust} (Dupac et al. 2003)), and found that this only reduced the fraction of excess emission at 33 GHz from 62 % to 48 %. This confirms that there is an excess of emission observed with the VSA at 33 GHz that cannot be explained by either free–free or thermal dust emission. Therefore to fit the 33 GHz data point, a peaked spectrum is required.

Peaked spectra can be caused by emission from ultra-compact (UC) HII regions, gigahertz-peaked spectra (GPS), magnetic dipole emission or electric dipole emission. UCHII regions are very compact, optically thick, HII regions while GPS are radio sources at high redshifts with synchrotron self–absorption. A detailed search of the *IRAS* point source catalogue (Beichman et al. 1988) revealed that there are only a few sources (< 4 %), within 1° of the centre of our image, that meet the colour criterion set by Wood & Churchwell (1989a) for UCHII regions. Further analysis reveals that to fit the data with emission from an UCHII region would require an emission measure of $\approx 2 \times 10^9$ cm^{-6}pc and an angular size of $\leqslant 1''$. These parameters are towards the upper end of the observed values for UCHII regions (Wood & Churchwell 1989b), and also imply that UCHII regions would appear as point–like sources in our image, which is not the case. We would also expect GPS to appear as point–like sources in our image, and to be visible in the NVSS and GB6 surveys discussed in Section 4.1. Neither of these are true.

Magnetic dipole emission has been ruled out due to polarization observations of the region by Battistelli et al. (2006).

Therefore, having ruled out UCHII regions, GPS and magnetic dipole emission as viable options, we have fitted a Draine & Lazarian (1998) spinning dust model for electric dipole radiation. Since we only have the one data point at 33 GHz, we fitted a linear combination of the models for the cold neutral medium and the dense molecular cloud (0.5CNM + 0.5MC) to ensure the peak occurred at 33 GHz. Clearly more data in the frequency range 5 – 60 GHz are required to confirm this fit.

6.2 Dust Emissivities

The dust emissivity, the ratio between the microwave and FIR emission, provides a convenient way[6] to represent the excess emission found in Fig. 5 and is measured in units of μK (MJy sr^{-1})$^{-1}$. Using the values in Table 6, the dust emissivity between 33 GHz and 100 μm was calculated for all 5 features and are tabulated in Table 7. Also listed in Table 7 is the dust emissivity for 6 other sources: 2 values based on HII regions and 4 values for typical intermediate Galactic latitudes.

The radio emissivity of dust at ≈ 30 GHz is known to have a typical value of ≈ 10 μK (MJy sr^{-1})$^{-1}$ with a factor of ≈ 2 variation at intermediate Galactic latitudes (Davies et al. 2006). The dust emissivity for the 5 features analysed in this work are consistent with this value. Comparing the dust emissivities listed in Table 7, we find that the features

[6] We note that for a given microwave intensity, the dust emissivity relative to the 100 μm intensity is a strong function of temperature.

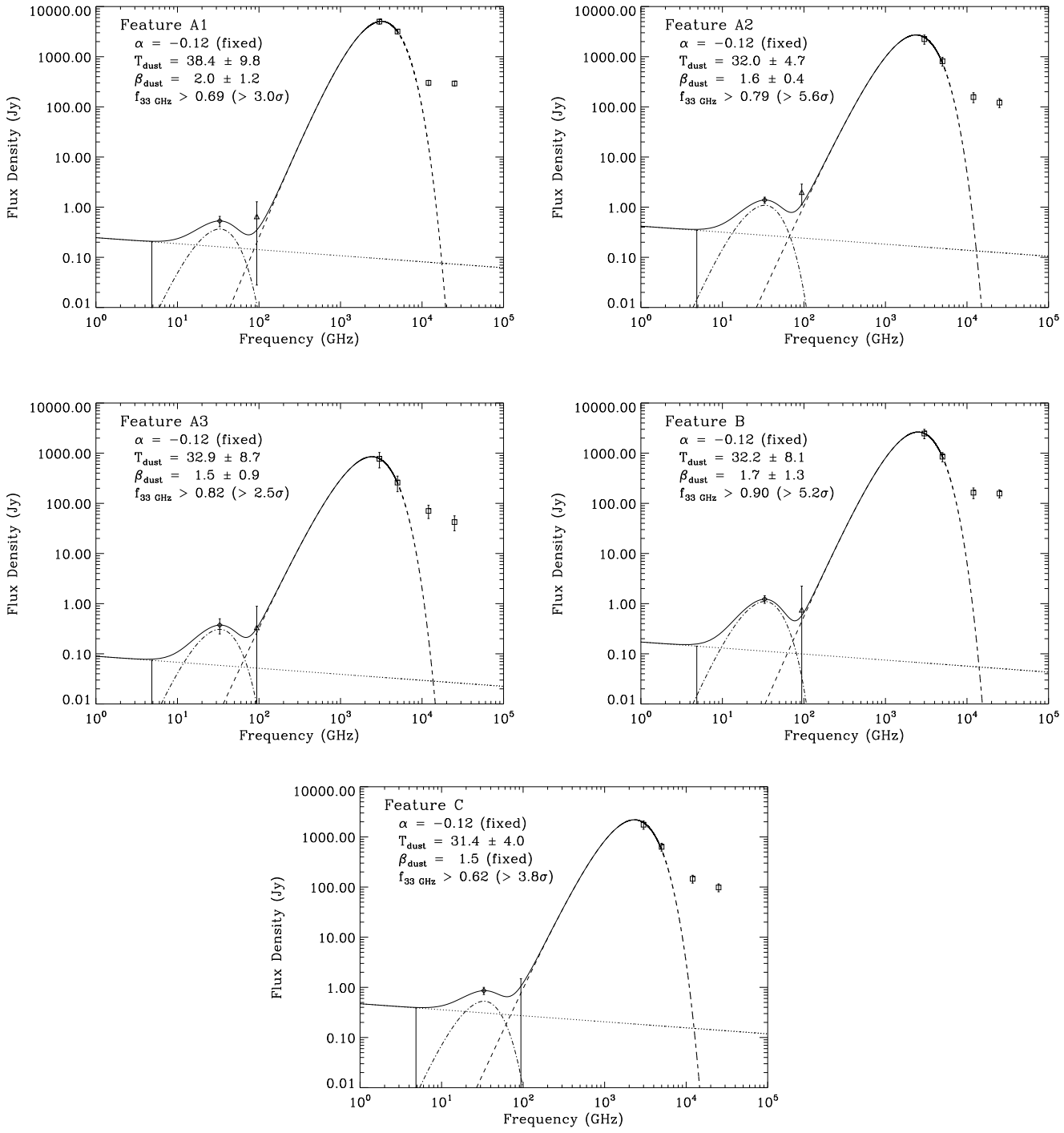

Figure 5. Integrated flux density spectra for the 5 features shown in Fig. 2a. A power-law with spectral index $\alpha = -0.12$ is plotted to represent the free–free emission 3σ upper limit (dotted line) and a modified black-body curve, fitted to the 94 GHz, 100 μm and 60 μm data points, is plotted to represent the thermal dust emission (dashed line). The best-fitting values for T_{dust} and β_{dust} are displayed on each plot individually. For feature C, the 94 GHz data point was only an upper limit, and therefore the modified black-body curve is fitted with a fixed dust emissivity value of $\beta_{dust} = 1.5$. The VSA 33 GHz data point is not accounted for by either of these curves and is fitted by a linear combination (0.5CNM + 0.5MC) of Draine & Lazarian (1998) spinning dust models (dash-dot line). The fraction of excess emission at 33 GHz ($f_{33\ GHz}$), and the corresponding significance, is displayed on each plot. Also plotted are the 25 μm and 12 μm data points, but these were not included in the SED fitting procedure.

Table 7. Dust emissivities at ≈ 30 GHz relative to 100 μm for the 5 features observed in this work, and 6 other sources to provide a comparison. The 6 HII regions is a mean value based on 6 southern HII regions, LPH 96 is also an HII region and LDN 1622 is a dark cloud. The all-sky value is a mean value outside the Kp2 mask, and the 15 regions value is a mean value of 15 high latitude regions both from *WMAP*. G159.6–18.5 is the value obtained with the COSMOSOMAS observations.

Source	Dust Emissivity μK (MJy sr^{-1})$^{-1}$	Reference
A1	2.8 ± 0.7	This paper
A2	16.4 ± 4.1	This paper
A3	12.8 ± 6.1	This paper
B	13.2 ± 3.6	This paper
C	13.0 ± 3.2	This paper
6 HII regions	3.3 ± 1.7	Dickinson et al. (2007)
LPH96	5.8 ± 2.3	Dickinson et al. (2006)
All–sky	10.9 ± 1.1	Davies et al. (2006)
15 regions	11.2 ± 1.5	Davies et al. (2006)
LDN1622	24.1 ± 0.7	Casassus et al. (2006)
G159.6–18.5	15.7 ± 0.3	Watson et al. (2005)

A2, A3, B and C have a dust emissivity similar to the typical value found for intermediate Galactic latitudes, while feature A1, with a much lower dust emissivity, is similar to that for HII regions.

The lower dust emissivity per unit of 100 μm surface brightness in HII regions may be the result of the relative difference in physical environmental conditions compared with those in the general ISM. For example, the warmer dust resulting from the strong UV radiation field in an HII region will emit more strongly at 100 μm, thereby reducing the radio to FIR emissivity ratio for a given amount of dust. Also the more energetic radiation field may disassociate the VSGs/PAHs responsible for the spinning dust emission. Feature A1, associated with IC 348, has an emissivity similar to an HII region although no HII region with a flux density greater than 200 mJy at 4.85 GHz is seen at the position of IC 348. Nevertheless, there is a significant UV radiation field arising from the low mass stars comprising the open cluster in the IC348 reflection nebulosity and there may additionally be some UV illumination from the nearby Perseus OB2 association. The overall radiation field in IC 348 is 10 – 100 times that of the general ISM (Bachiller et al. 1987). The higher dust temperature ($T_{dust} \approx 40$ K) compared with that ($T_{dust} \approx 30$ K) in the cooler features confirms the presence of this higher radiation field in the A1 region, but the lack of a detectable HII region indicates a less intense radiation field or a lower gas density than in a normal HII region.

Ignoring feature A1, with its lower dust emissivity, the mean dust emissivity calculated for features A2, A3, B and C is 13.8 ± 2.0 μK (MJy sr^{-1})$^{-1}$, which is consistent with the integrated value calculated for the whole region by Watson et al. (2005). These comparisons of dust emissivity confirm that our measurement of excess emission is in agreement with previous observations at intermediate Galactic latitudes, and can be explained in terms of spinning dust.

6.3 Anomalous Emission and Angular Scale

G159.6–18.5 was observed by Watson et al. (2005) with the COSMOSOMAS experiment on angular scales of $\approx 1^o$, and hence could not resolve any of the 5 individual features observed with the VSA in this present work. Using both results allow us to investigate how the anomalous emission varies with angular scale. The total *WMAP* flux density measured by Watson et al. (2005) was 40.3 ± 0.4 Jy at 33 GHz, and the total flux density in the 5 features in the VSA map was found to be 4.4 ± 0.4 Jy (Table 6). This implies that the VSA is only observing a small fraction (≈ 10 %) of the anomalous emission observed by COSMOSOMAS, and that the bulk of the anomalous emission is originating from large scale structure that is resolved out by the VSA. This idea also explains why the integrated flux density in the filtered VSA image, 0.96 ± 0.12 Jy (Table 5), is much lower than the flux density in the unfiltered VSA image. Therefore, the features observed by the VSA must be "peaks" of anomalous emission, located on a large scale, diffuse cloud responsible for the 33 GHz emission in *WMAP*.

7 CONCLUSIONS

Observations of G159.6–18.5 with the VSA in its super-extended array configuration with a synthesized beam of ≈ 7′ FWHM provide clear evidence for excess emission at 33 GHz in 5 distinct dust-correlated components. This anomalous emission cannot be explained by either free–free or thermal dust emission, and requires a peaked spectrum. After ruling out both UCHII regions and GPS by observations of ancillary data, and magnetic dipole emission based on previous observations (Battistelli et al. 2006), we explain the excess emission as electric dipole radiation (spinning dust) as predicted by Draine & Lazarian (1998).

The dust emissivity for all 5 features was found to be in agreement with the values from previous observations. Feature A1, associated with the reflection nebula IC 348, was found to have a similar value to that of HII regions, while the other 4 features all agree with the typical value for intermediate Galactic latitudes.

By performing a correlation analysis between the FIR emission and the microwave emission, we found a strong correlation (≈ 0.80), which suggests that the microwave emission is related to the dust. This correlation analysis also showed that it is only the 5 features observed with the VSA that are highly correlated, and not the background emission, which was found to have a correlation coefficient of ≈ 0.17. This strongly suggests that it is only the anomalous emission that is highly correlated with the FIR, and we therefore interpret this emission as spinning dust. Spectroscopic observations (Iglesias-Groth et al. 2008) have provided evidence for the existence of the naphthalene cation (a simple PAH) in the G159.6–18.5 region, which could be responsible for this spinning dust.

To gain a better understanding of the origin and physical nature of this anomalous emission, we compared our results with the previous analysis of this region performed by Watson et al. (2005). This analysis revealed that the bulk of this anomalous emission (≈ 90 %) appears to originate from large scale structure, which is resolved out by the

VSA. We therefore conclude that the anomalous emission in G159.6–18.5 is very diffuse and not concentrated in the 5 features observed with the VSA.

Future high-resolution observations at microwave wavelengths, combined with the *Spitzer* IR data, is needed to investigate in more detail the nature of the anomalous emission. The *Planck* and *Herschel* satellites will provide data in the microwave, sub-mm and FIR regimes which are required to measure the spectrum of anomalous dust in the frequency range $\approx 10 - 100$ GHz.

ACKNOWLEDGMENTS

CTT acknowledges an STFC studentship. CD acknowledges an STFC Advanced Fellowship. We thank an anonymous referee for useful comments, which led to significant improvements in this paper.

REFERENCES

Ali-Haïmoud Y., Hirata C. M., Dickinson C., 2009, MNRAS, 395, 1055
Ami Consortium: Scaife A. M. M. et al., 2009a, MNRAS, 394, L46
Ami Consortium: Scaife A. M. M. et al., 2009b, arXiv:0908.1655
Andersson B.-G., Wannier P. G., Moriarty-Schieven G. H., Bakker E. J., 2000, AJ, 119, 1325
Bachiller R., Guilloteau S., Kahane C., 1987, A&A, 173, 324
Banday A. J., Dickinson C., Davies R. D., Davis R. J., Górski K. M., 2003, MNRAS, 345, 897
Battistelli E. S., Rebolo R., Rubiño-Martín J. A., Hildebrandt S. R., Watson R. A., Gutiérrez C., Hoyland R. J., 2006, ApJ, 645, L141
Beichman C. A., Neugebauer G., Habing H. J., Clegg P. E., Chester T. J., 1988, Infrared astronomical satellite (IRAS) catalogs and atlases. Volume 1: Explanatory supplement, 1
Bennett C. L., Halpern M., Hinshaw G. et al., 2003, ApJS, 148, 1
Casassus S., Cabrera G. F., Förster F., Pearson T. J., Readhead A. C. S., Dickinson C., 2006, ApJ, 639, 951
Cernicharo J., Bachiller R., Duvert G., 1985, A&A, 149, 273
Condon J. J., Broderick J. J., Seielstad G. A., 1989, AJ, 97, 1064
Condon J. J., Cotton W. D., Greisen E. W., Yin Q. F., Perley R. A., Taylor G. B., Broderick J. J., 1998, AJ, 115, 1693
Davies R. D., Dickinson C., Banday A. J., Jaffe T. R., Górski K. M., Davis R. J., 2006, MNRAS, 370, 1125
de Oliveira-Costa A., Kogut A., Devlin M. J., Netterfield C. B., Page L. A., Wollack E. J., 1997, ApJ, 482, L17
de Oliveira-Costa A., Tegmark M., Gutierrez C. M., Jones A. W., Davies R. D., Lasenby A. N., Rebolo R., & Watson R. A., 1999, ApJ, 527, L9
de Oliveira-Costa A., Tegmark M., Finkbeiner D. P. et al., 2002, ApJ, 567, 363
Desert F.-X., Boulanger F., Puget, J. L., 1990, A&A, 237, 215
Dickinson C., Davies R. D., Davis R. J., 2003, MNRAS, 341, 369
Dickinson C., Battye R. A., Carreira P. et al., 2004, MNRAS, 353, 732
Dickinson C., Casassus S., Pineda J. L., Pearson T. J., Readhead A. C. S., Davies, R. D., 2006, ApJ, 643, L111
Dickinson C., Davies R. D., Bronfman L., Casassus S., Davis R. J., Pearson T. J., Readhead A. C. S., Wilkinson P. N., 2007, MNRAS, 379, 297
Dickinson C., Davies R. D., Allison J. R. et al., 2009, ApJ, 690, 1585
Dobler G., Finkbeiner D. P., 2008, ApJ, 680, 1222
Draine B. T., Lazarian A., 1998, ApJ, 508, 157
Draine B. T., Lazarian A., 1999, ApJ, 512, 740
Dupac, X., Bernard J.-P., Boudet N. et al., 2003, A&A, 404, 11
Fiedler R., Pauls T., Johnston K. J., Dennison B., 1994, ApJ, 430, 595
Finkbeiner D. P., 2003, ApJS, 146, 407
Finkbeiner D. P., 2004, ApJ, 614, 186
Finkbeiner D. P., Schlegel, D. J., Frank C., Heiles C., 2002, ApJ, 566, 898
Grainge, K., Carreira P., Cleary K. et al., 2003, MNRAS, 341, L23
Hafez Y. A., Davies R. D., Davis R. J. et al. 2008, MNRAS, 388, 1775
Hildebrandt S. R., Rebolo R., Rubiño-Martín J. A., Watson R. A., Gutiérrez C. M., Hoyland R. J., Battistelli E. S., 2007, MNRAS, 382, 594
Hill R. S., Weiland J. L., Odegard N. et al., 2009, ApJS, 180, 246
Hinshaw G., Weiland J. L., Hill R. S. et al., 2009, ApJS, 180, 225
Högbom J. A., 1974, A&AS, 15, 417
Iglesias-Groth S., Manchado A., García-Hernández D. A., González Hernández J. I., Lambert D. L., 2008, ApJ, 685, L55
Kogut A., Banday A. J., Bennett C. L., Gorski K. M., Hinshaw G., Smoot G. F., Wright E. I., 1996, ApJ, 464, L5
Leitch E. M., Readhead A. C. S., Pearson T. J., Myers S. T., 1997, ApJ, 486, L23
Miville-Deschênes M.-A., Lagache G., 2005, ApJS, 157, 302
Miville-Deschênes M.-A., Ysard N., Lavabre A., Ponthieu N., Macías-Pérez J. F., Aumont J., Bernard J. P., 2008, A&A, 490, 1093
Pauls T., Schwartz P. R., 1989, in Winnewisser G., ed., The Physics and Chemistry of Interstellar Molecular Clouds - mm and Sub-mm Observations in Astrophysics, Springer-Verlag, Berlin, 331, 225
Reich P., Reich W., 1986, A&AS, 63, 205
Reich W., Reich P., 2009, IAU Symposium, 259, 603
Ridge N. A., Di Francesco J., Kirk H. et al., 2006a, AJ, 131, 2921
Ridge N. A., Schnee S. L., Goodman A. A., Foster J. B., 2006b, ApJ, 643, 932
Scott P. F., Carreira P., Cleary K. et al., 2003, MNRAS, 341, 1076
Waldram E. M., Pooley G. G., Grainge K. J. B., Jones M. E., Saunders R. D. E., Scott P. F., Taylor A. C., 2003,

MNRAS, 342, 915
Watson R. A., Carreira P., Cleary K. et al., 2003, MNRAS, 341, 1057
Watson R. A., Rebolo R., Rubiño-Martín J. A., Hildebrandt S., Gutiérrez C. M., Fernández-Cerezo S., Hoyland R. J., Battistelli E. S., 2005, ApJ, 624, L89
Wood D. O. S., Churchwell E., 1989a, ApJ, 340, 265
Wood D. O. S., Churchwell E., 1989b, ApJS, 69, 831

This paper has been typeset from a TEX/ LATEX file prepared by the author.